Journal of
Materials Chemistry C

ROYAL SOCIETY
OF CHEMISTRY

PAPER

View Article Online
View Journal | View Issue

Cite this: *J. Mater. Chem. C*, 2022, **10**, 17127

Chiral coordination compounds with exceptional enantioselectivity†

Minju Lee and Kang Min Ok*

Systematic discovery of crystalline materials with noncentrosymmetric (NCS) structures revealing the structure-derived functional properties is an ongoing challenge. Two Zn-based chiral coordination compounds, $[Zn_2((R,R)\text{-TBPG})_2(H_2O)_5]\cdot4H_2O$ [(*R*)-Zn] and $[Zn_2((S,S)\text{-TBPG})_2(H_2O)_5]\cdot4H_2O$ [(*S*)-Zn] (TBPG = terephthaloyl-bis-phenyl glycine), were successfully synthesized *via* mild solvothermal reactions with the aid of the newly designed chiral organic ligands. (*R*)-Zn and (*S*)-Zn crystallizing in the NCS polar space group, $P2_1$, present very rare bilayer structures attributed to the strong π–π and hydrogen bonding interactions. Powder second harmonic generation (SHG) measurements indicate that (*R*)-Zn and (*S*)-Zn reveal SHG intensities of about 0.5 times that of KH_2PO_4 under 1064 nm radiation. The title compounds are very stable in a variety of different solvents in wide pH ranges. Surprisingly, ethyl alcohol is produced if crystals of the reported homochiral compound are immersed in diethyl ether. The homochiral title compounds also reveal exceptionally enantioselective sensing behavior toward the chiral amino acid, histidine. A plausible mechanism for the enantioselective discrimination of the reported materials is also proposed.

Received 23rd September 2022,
Accepted 28th October 2022

DOI: 10.1039/d2tc04016f

rsc.li/materials-c

Introduction

Second-order nonlinear optical (NLO) materials have been playing a critical role in many optical applications such as medical lasers, delicate processes in photolithography, optical communication systems, *etc.*[1–3] Viable second-order NLO materials must satisfy several important requirements including relevant transparency range, high laser-induced damage threshold, chemical stability, and crystallographically noncentrosymmetric (NCS) structure. Although all the conditions are equally important, systematically preparing crystalline materials with NCS structures has been found to be extremely difficult because of nature's preference on symmetry. A number of efforts have been made to improve the probability of functional NLO materials with NCS structures.[4–6] Among many, one promising approach has been considered to introduce the so called NCS chromophores such as second-order Jahn–Teller distortive cations (Pb^{2+}, Sb^{3+}, Ti^{4+}, Mo^{6+}, *etc.*),[7–10] greatly polarizable d^{10} metal cations (Zn^{2+}, Cd^{2+}, *etc.*),[11–13] and π-delocalized anionic units (CO_3^{2-}, BO_3^{3-}, NO_3^{-}, *etc.*) during the initial synthesis step.[14–16] Unfortunately, however, structures of the major crystalline products obtained from the aforementioned strategy still turned out to be centrosymmetric, possibly because the asymmetric units prefer to line up in an antiparallel manner. Besides, it is almost impossible to control the centricity of the products obtained under various synthetic conditions. Recently, our research group has been very successful with systematic syntheses of many NCS organic–inorganic hybrid compounds and/or coordination polymers (CPs) by using chiral organic structure-directing agents, in which the chiral templates induce the alignment of the asymmetric inorganic units and result in extended structures with macroscopic NCS structures.[17–21] Unlike solid-state materials with pure inorganic elements, CPs with more controllable coordination modes tend to be rather rationally designed and synthesized under milder conditions.[22,23] In addition, CPs normally reveal much flexible structures such as infinite chains (1D), layers (2D), and three-dimensional (3D) networks.[24] Attributable to the unique structural features, CPs have been proven to be very interesting materials with a variety of applications such as gas storage/separation, catalysts, and sensors.[25–29] In this work, we have synthesized two chiral CPs with novel NCS structures, $[Zn_2((R,R)\text{-TBPG})_2(H_2O)_5]\cdot4H_2O$ [(*R*)-Zn] and $[Zn_2((S,S)\text{-TBPG})_2(H_2O)_5]\cdot4H_2O$ [(*S*)-Zn], using the highly polarizable d^{10} metal cation, Zn^{2+}, and the newly designed phenylglycine-based chiral organic ligands. Interestingly, the reported chiral CPs exhibit excellent enantioselective discrimination behavior toward the chiral amino acid, histidine. As an

---

Department of Chemistry, Sogang University, Seoul 04107, Republic of Korea.
E-mail: kmok@sogang.ac.kr

† Electronic supplementary information (ESI) available: Experimental details, crystallographic data, selected bond distances and angles, PXRD patterns, EDX, infrared, and UV-vis spectra, TGA diagrams, CD-spectra, band structures, SHG plots, dipole moments, GC-MS results, fluorescence emission spectra, and Stern–Volmer plots. CCDC 2204911–2204913. For ESI and crystallographic data in CIF or other electronic format see DOI: **https://doi.org/10.1039/d2tc04016f**

essential amino acid, histidine is responsible for a wide range of physiological processes in the human body.[30] Accordingly, various techniques for the separation of histidine have been developed.[31–33] Although many metal organic frameworks (MOFs) and CPs have been developed so far, detailed studies on enantioselective fluorescence sensing have not been conducted yet. In this work, chiral CPs revealing excellent enantioselective discrimination for L/D-histidine are introduced.

Results and discussion

Colorless crystals of the two new Zn-based CPs, (*R*)-Zn and (*S*)-Zn, were grown through mild hydrothermal reactions at 80 °C (ESI†). Single-crystal X-ray diffraction (SC-XRD) indicates that both (*R*)-Zn and (*S*)-Zn crystallize in the monoclinic polar NCS space group, $P2_1$ (no. 4). Interestingly, the chirality of the (*R*)-Zn and (*S*)-Zn has been driven by the corresponding chiral organic ligands, (*R*,*R*)- and (*S*,*S*)-TBPG, respectively. Although the two title compounds are enantiomers, their structural backbones are the same except for the absolute configurations. Thus, only a detailed structural description of (*R*)-Zn is presented here. The asymmetric unit of (*R*)-Zn contains two Zn^{2+} cations, two $TBPG^{2-}$ ligands, five coordinated water ligands, and four lattice water molecules (Fig. 1). The carboxylates in the $TBPG^{2-}$ ligands linked to the Zn^{2+} cations reveal two kinds of coordination modes, *i.e.*, a monodentate and a *syn–syn* bidentate bridging mode. Zn_1 and Zn_2 are bridged by one water molecule and two $TBPG^{2-}$ ligands (Fig. S2, ESI†). Each Zn^{2+} cation is coordinated by six O atoms from three different carboxylate groups of $TBPG^{2-}$ ligands and three H_2O molecules, which results in slightly distorted ZnO_6 octahedra (Fig. S2, ESI†). The observed Zn–O lengths and O–Zn–O angles are in the range of 2.027(4)–2.287(6) Å and 83.1(2)–177.2(2)°, respectively (Tables S2–S5, ESI†). Right- and left-handed helical chains are generated once $TBPG^{2-}$ ligands bridge Zn_1–Zn_2 along the *b*-axis in (*R*)-Zn and (*S*)-Zn, respectively (Fig. 2a). Other right- and left-handed helical chains are also observed if $TBPG^{2-}$ ligands bridge Zn_1–Zn_2 along the *c*-axis in (*R*)-Zn and (*S*)-Zn, respectively (Fig. 2b). The linkage of the helical chains running along the *b*- and *c*-axis results in the layered backbones for the title compounds in the *bc*-plane (Fig. 2c). Interestingly, a unique bilayer structure is further induced *via* π–π stacking and hydrogen bonding interactions between the two types of layers (see green and purple layers in Fig. 3a). The benzene rings of the $TBPG^{2-}$ ligands (green) form π–π stacking interactions with the adjacent $TBPG^{2-}$ ligands (purple) at a distance of 3.865 Å (Fig. 3b). In addition, hydrogen bonds occur between hydrogen of the water molecules in one layer (green/purple) and oxygen of the carboxyl groups in the other layer (purple/green), in which the observed O···H distances are 2.743 Å and 2.799 Å (Fig. 3b). The CALC SOLV command in the PLATON software suggests that (*R*)-Zn possesses about 5% of void space.[34] However, if the lattice and coordinated water molecules are excluded, the void space increases to 15%.

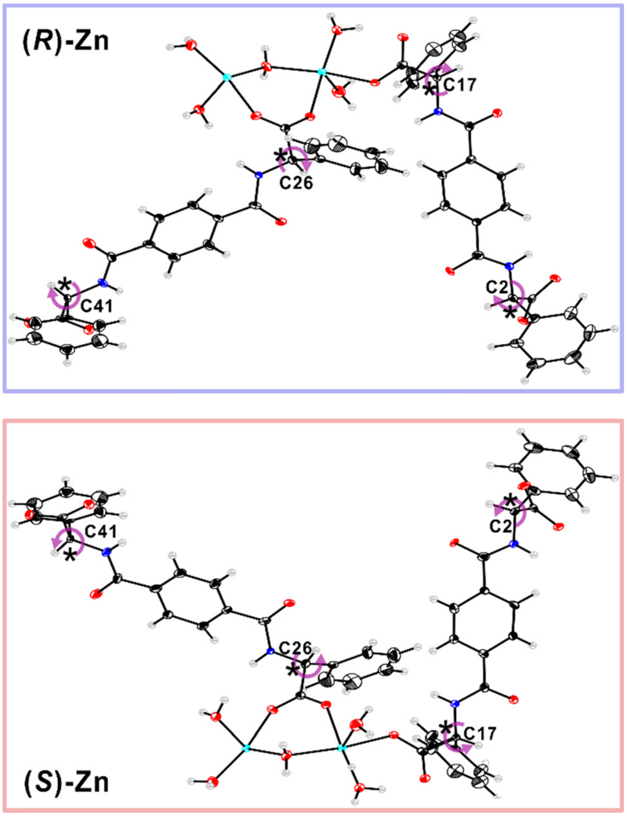

Fig. 1 ORTEP (50% probability ellipsoids) drawings for (*R*)-Zn and (*S*)-Zn. Chiral carbons, C2, C17, C26, and C41, are marked with asterisks (*) (cyan, Zn; black, C; gray, H; blue, N; red, O).

The phase purity of (*R*)-Zn and (*S*)-Zn was confirmed by powder X-ray diffraction (PXRD) (Fig. S3, ESI†). The atomic ratios determined by energy dispersive X-ray analysis are also similar to those obtained by SC-XRD analysis (Fig. S4, ESI†).

The IR spectra of (*R*)-Zn and (*S*)-Zn mainly exhibit vibrations arising from the coordinated TBPG ligands. Broad overlapped peaks emerging at *ca.* 3000–3600 cm^{-1} are due to the N–H and O–H stretching vibrations for secondary amines and water molecules, respectively. Several peaks observed at *ca.* 1730–1680, 1680–1630, 1630–1550, and 1525–1400 cm^{-1} can be assigned to the C═O stretching of carboxylic acid, C═O stretching of the amide, N–H bending of the amide, and asymmetric/symmetric stretching of the carboxylate groups, respectively. While peaks found at *ca.* 850–690 cm^{-1} can be assigned to the C–H out-of-plane bending vibrations in the benzene ring of ligands, those occurring at *ca.* 600–500 cm^{-1} are attributed to the Zn–O bonds (Fig. S5, ESI†).[35]

Ultraviolet-visible (UV-vis) diffuse reflectance spectra of the (*R*,*R*)-TBPG, (*S*,*S*)-TBPS, (*R*)-Zn, and (*S*)-Zn exhibit steep slopes at around 310 nm. As seen in Fig. S6 (ESI†), the obtained UV-vis spectra for the TBPG ligands and the title compounds are very similar. However, (*R*)-Zn and (*S*)-Zn were slightly red-shifted upon coordination because of the interactions between ligands and metals. The optical band gaps of the TBPG ligands and (*R*)/(*S*)-Zn, converted from the reflectance data *via* the Kubelka–Munk function,[36] are *ca.* 4.03 and 3.98 eV, respectively (Fig. S6, ESI†), which might be due to the inter-ligand charge

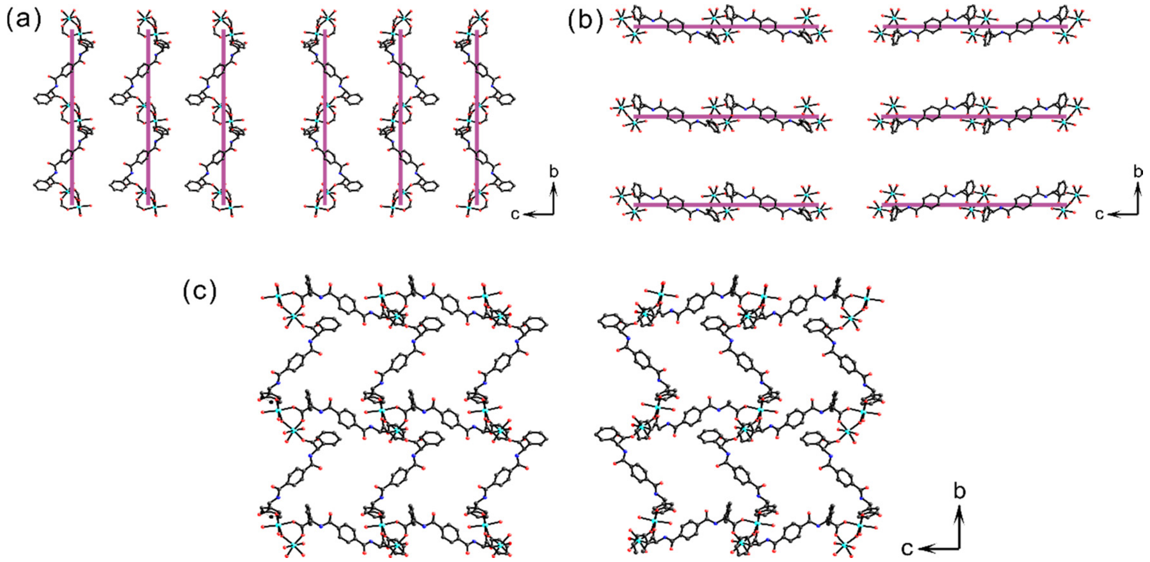

Fig. 2 (a) Right and left-handed 1D helical chains in (*R*)-Zn (left) and (*S*)-Zn (right) along the *b*-axis. (b) Right and left-handed 1D helical chains in (*R*)-Zn (left) and (*S*)-Zn (right) along the *c*-axis. (c) Layered structures of (*R*)-Zn (left) and (*S*)-Zn (right) in the *bc*-plane. H atoms are removed for clarity.

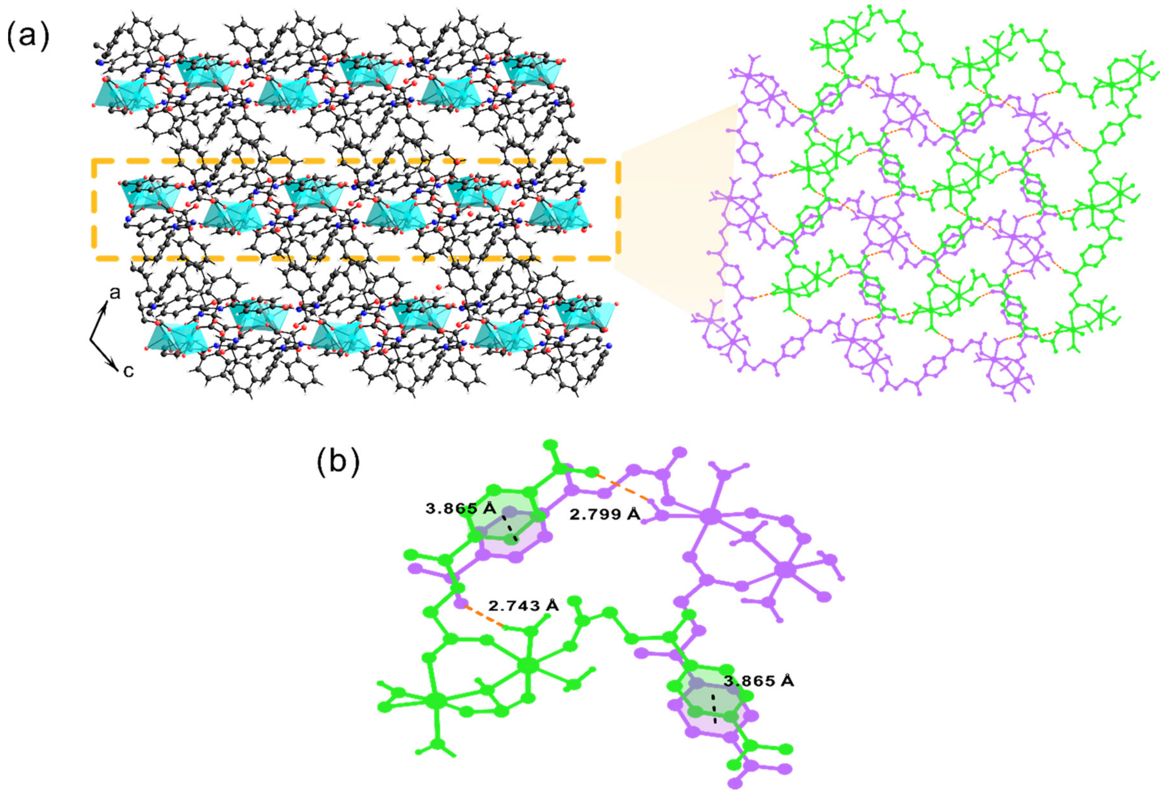

Fig. 3 (a) Ball-and-stick and polyhedral representations of (*R*)-Zn in the *ac*-plane (cyan, Zn; black, C; light gray, H; blue, N; red, O). A bilayer structure is observed through the π–π stacking and hydrogen bonding interactions (orange dotted lines). (b) The π–π stacking at a distance of 3.865 Å and the hydrogen bonding interactions at a distance of 2.743 and 2.799 Å are observed between the two types of layers (green and purple).

transfer between TBPG ligands or the ligand to metal charge transfer between ligands and metals.[37,38]

The thermal stability of (*R*)-Zn and (*S*)-Zn was investigated by thermogravimetric analysis (TGA) (Fig. S7, ESI†). Initially, (*R*)-Zn and (*S*)-Zn reveal weight losses of *ca.* 13.8% and 13.3% from 50 °C to 130 °C by losing lattice and coordinated water molecules (calc. 14.1%). Upon further heating, frameworks of (*R*)-Zn and (*S*)-Zn start collapsing and exhibit further weight losses of *ca.* 72.7% and 73.6% above 300 °C due do the thermal decomposition of the TBPG ligands (cal. 74.2%). The thermally decomposed residues above 490 °C were identified as ZnO based on the PXRD pattern (Fig. S8, ESI†).

Although the absolute configurations of the reported chiral CPs have been well-determined by SC-XRD (Fig. 1), the chirality was further confirmed by solid-state CD spectroscopy. The chiral ligands, (*R*,*R*)-TBPG and (*S*,*S*)-TBPG, clearly display opposite CD signals at *ca.* 238–325 nm. In addition, the title chiral compounds, (*R*)-Zn and (*S*)-Zn, dictated by the corresponding chiral ligands also exhibit opposite CD signals at *ca.* 225–325 nm (Fig. S9a, ESI†). Because of the coordination between metals and ligands, the CD signals of the (*R*)-Zn and (*S*)-Zn are slightly red-shifted.

The band structures and density of states (DOS) of the title compounds were calculated using the structural data obtained by SC-XRD. Through the DFT-based electron band structure calculations, the band gaps of (*R*)-Zn and (*S*)-Zn were calculated to be 3.22 eV and 3.20 eV, respectively (Fig. S10, ESI†). The calculated band gaps are smaller than those of the experimentally measured values of 3.98 eV for (*R*)-Zn and (*S*)-Zn. It is well known that the calculated band gaps are underestimated compared to those of experimental data.[39] Band structure calculations also indicate that both (*R*)-Zn and (*S*)-Zn reveal direct band gaps. In the DOS, the valence band maximum primarily consists of 2p orbitals from C, N, and O. On the other hand, the conduction band minimum is mainly composed of 2p orbitals from C (Fig. S11, ESI†). Therefore, the inter-ligand charge transfer of the p orbitals in TBPG ligands mainly determines the band gap.

Powder SHG measurements suggest that (*R*)-Zn and (*S*)-Zn exhibit mild SHG efficiencies of *ca.* 0.5 times that of KH_2PO_4 and are type-I phase-matchable (Fig. S12, ESI†). To understand the structural influence on the measured SHG efficiency, dipole moment calculations for the constituting ZnO_6 octahedra were performed (Table S6, ESI†). Since the title compounds crystallize in the monoclinic polar space group, $P2_1$, the contributions from the *x*- and *z*-components to the net moment would be negligible; however, the contribution of the *y*-component to the net dipole moment would be significant. Our calculations indicate that the title compounds exhibit a net dipole moment of 1.87 D along the *b*-direction, which should be responsible for the observed mild SHG efficiency (Fig. S13, ESI†).

Stability under various conditions is an important factor for materials' practical applications. Therefore, the stability of the title compounds in various solvents including water under various pH conditions was systematically investigated. PXRD measurements were carried out for polycrystalline samples of (*R*)-Zn immersed in various solvents and pH ranges for 2 d at RT (Fig. S14, ESI†). As seen in Fig. S14 (ESI†), (*R*)-Zn is very stable in a variety of solvents including water in a wide range of pH values based on PXRD. The excellent chemical stability in various organic solvents as well as in a wide pH range in aqueous solutions is attributed to the strong intermolecular π–π stacking interactions in the structures.[40]

To investigate a possible exchange of lattice water molecules with other solvents, crystals of (*S*)-Zn have been soaked in distilled diethyl ether under an argon atmosphere for 1 d. Interestingly, SC-XRD on the immersed crystal in diethyl ether indicates that one of the lattice waters, O20, present in the original (*S*)-Zn crystal was changed to ethanol (Fig. 4). Through gas chromatography-mass spectrometry (GC-MS), we also found that both diethyl ether and ethanol existed in the solvent containing the (*S*)-Zn crystals for 1 d (Fig. S17, ESI†). In other words, ethanol was clearly observed from the single crystal of (*S*)-Zn as well as in the diethyl ether solvent. Although the soaking time of (*S*)-Zn crystals in the diethyl ether increases up to 14 d to check if more ethanol is produced, no significant change was monitored (Fig. S18–S21, ESI†). As seen from the obtained area percent in GC-MS data, almost similar amounts of ethanol and diethyl ether of *ca.* 9.4–13.6% and 86.4–80.6%, respectively, were detected although the soaking time of the crystals increases from 1 to 14 d. In addition, the same experiments were performed to test whether the transformation from diethyl ether to ethanol occurs using the crystalline $Zn(NO_3)_2$ or the free TBPG-ligand. However, ethanol was not detected at all in the absence of (*S*)-Zn under the same conditions (Fig. S22 and S23, ESI†). Thus, we believe that the role of (*S*)-Zn is critical for the hydrolysis of diethyl ether to ethanol.

(*R*)-Zn exhibits an emission at *ca.* 680 nm upon excitation at 340 nm in the solid-state fluorescence spectrum (Fig. S24, ESI†),

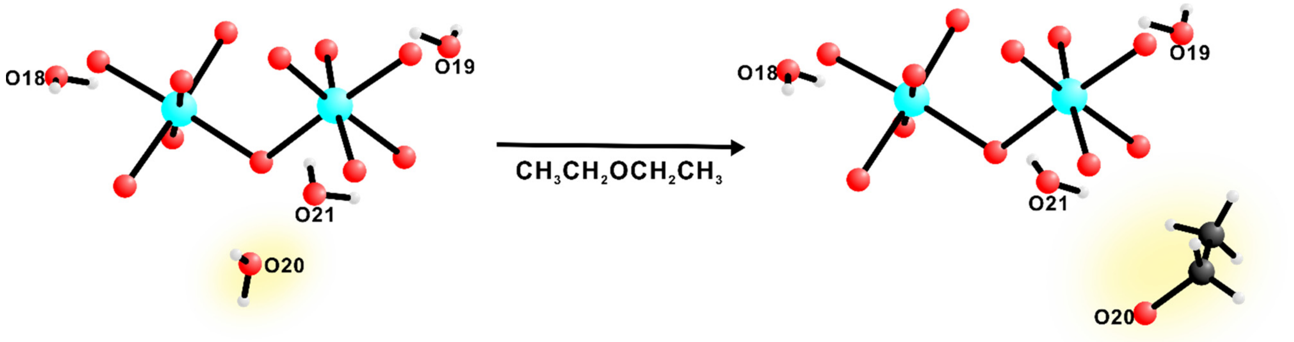

Fig. 4 Coordination environment of Zn^{2+} and lattice molecules before and after soaking (*S*)-Zn crystals in diethyl ether.

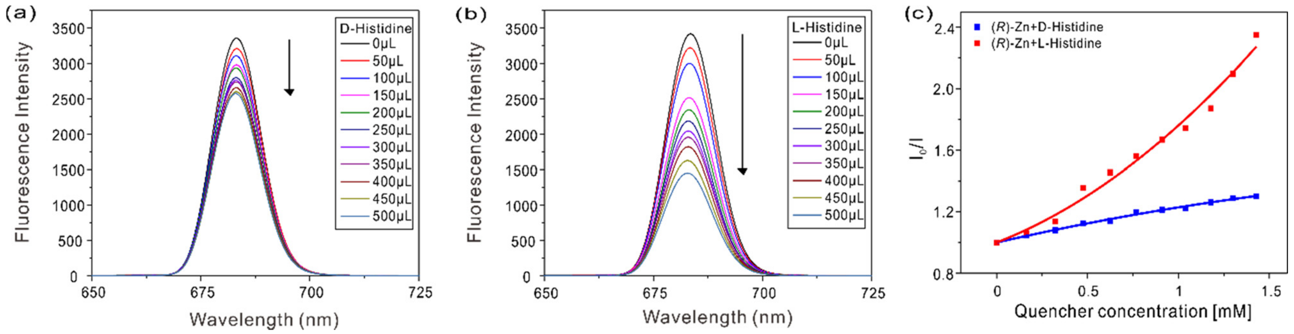

Fig. 5 Fluorescence emission spectra of (*R*)-Zn upon addition of (a) D- and (b) L-histidine, and Stern–Volmer (SV) plots (c) of (*R*)-Zn + D-histidine and (*R*)-Zn + L-histidine.

in which the fluorescence should be mainly derived from the (*R*,*R*)-TBPG ligand. Since (*R*)-Zn is homochiral and stable in water, the compound was tested for applicability in an enantioselective fluorescence sensor in aqueous solution. Interestingly, the decrease of fluorescence intensity was much greater upon adding L-histidine to the solution containing (*R*)-Zn (Fig. 5a and b). The fluorescence quenching clearly indicates that (*R*)-Zn recognizes L-histidine more enantioselectively than D-histidine. The fluorescence quenching efficiency was further analyzed using the Stern–Volmer (SV) equation, $I_0/I = K_{SV}[Q] + 1$, in which K_{SV} is the quenching constant, [Q] is the molar concentration of histidine, and I_0 and I are the fluorescence intensities before and after the addition of the histidine solution, respectively.[41,42] The K_{SV} constants calculated through the SV equations for D-histidine and L-histidine are 2.1×10^2 M^{-1} and 9.2×10^2 M^{-1}, respectively, in which the enantioselectivity of (*R*)-Zn + L-histidine over (*R*)-Zn + D-histidine is evident in the SV plots (Fig. 5c). Additionally, the enantioselectivity factor, α ($\alpha = K_{SV}$ (L-histidine)/K_{SV} (D-histidine)), is calculated to be 4.38, which is much better than those of recently reported chiral MOFs (Table 1).[43] The framework of (*R*)-Zn was robustly maintained even after the fluorescence experiment, which was confirmed through the PXRD measurement (Fig. S25, ESI†). In order to investigate the key factors responsible for the enantioselective discrimination of (*R*)-Zn, similar experiments were further conducted using the free (*R*,*R*)-TBPG ligand under the same conditions, from which the obtained K_{SV} constants for (*R*,*R*)-TBPG + D-histidine and (*R*,*R*)-TBPG + L-histidine turned out to be 4.3×10^2 M^{-1} and 7.0×10^2 M^{-1}, respectively, with the calculated enantioselectivity factor, α, of 1.63. Although the fluorescence quenching occurred by adding L- and D-histidine to the solutions containing the (*R*,*R*)-TBPG ligand, the free (*R*,*R*)-TBPG ligand alone does not show as clear enantioselectivity as the (*R*)-Zn (Fig. S26 and S27, ESI†). Thus, the rigid chiral backbone of (*R*)-Zn should be critical for the enantioselectivity, in which small chiral guest molecules can interact through the chiral framework. To identify the origin revealing the fluorescence quenching, further experiments were performed using imidazole, which is the specific functional group of histidine. Interestingly, we found that the fluorescence of (*R*)-Zn was well-quenched by the smaller imidazole (Fig. S28 and S29, ESI†). The observation suggests that the fluorescence is quenched through the interactions between (*R*)-Zn and the imidazole ring of histidine. The interactions are confirmed by additional peaks appearing in the ^{1}H NMR data for (*R*)-Zn + histidine solution, in which the deshielded peaks for histidine hydrogen atoms were shifted to the downfield (Fig. S30, ESI†). Considering all the experimental evidence, it can be concluded that the excellent enantioselective fluorescence sensing of (*R*)-Zn occurs *via* the interactions between the imidazole rings of chiral histidine and the rigid chiral backbones in (*R*)-Zn (Scheme 1).

Table 1 Comparison of the enantioselective factor of some reported fluorescent sensors

Host	Guest	K_{SV} constant (M)	Enantioselectivity factor, α	Ref.
$\{[Cd(L)(4,4'\text{-bipy})]\cdot DMA\cdot 5H_2O\}_n$	Penicillamine	1.4×10^3 5.1×10^3	3.64	43
CCOF-7-NSs	α-Pinene	3.95×10^2 1.35×10^3	3.41	44
$[Cd_2(L)(H_2O)_2]\cdot 6.5DMF\cdot 3EtOH$	2-Amino-3-methyl-1-butanol	0.53×10^3 1.7×10^3	3.12	45
$Eu^{3+}@\{[Me_2NH_2]_2[Zn_2(d\text{-}L)_2(HCO_2)(OH)]\cdot 5H_2O\}_n$	Ornidazole	9.1×10^3 2.4×10^4	2.64	46
$[Zn_3((S)\text{-}L1)(tma)_2(DMF)_3]\cdot 2\cdot DMF$	Mosher's acid	0.90×10^3 1.98×10^3	2.23	42
$[Zn_2(L)_{1.5}(H_2O)_2\cdot Me_2NH_2]$	Histidine	0.64×10^2 1.15×10^2	1.79	47
(*R*)-Zn	Histidine	2.1×10^2 9.2×10^2	4.38	This work

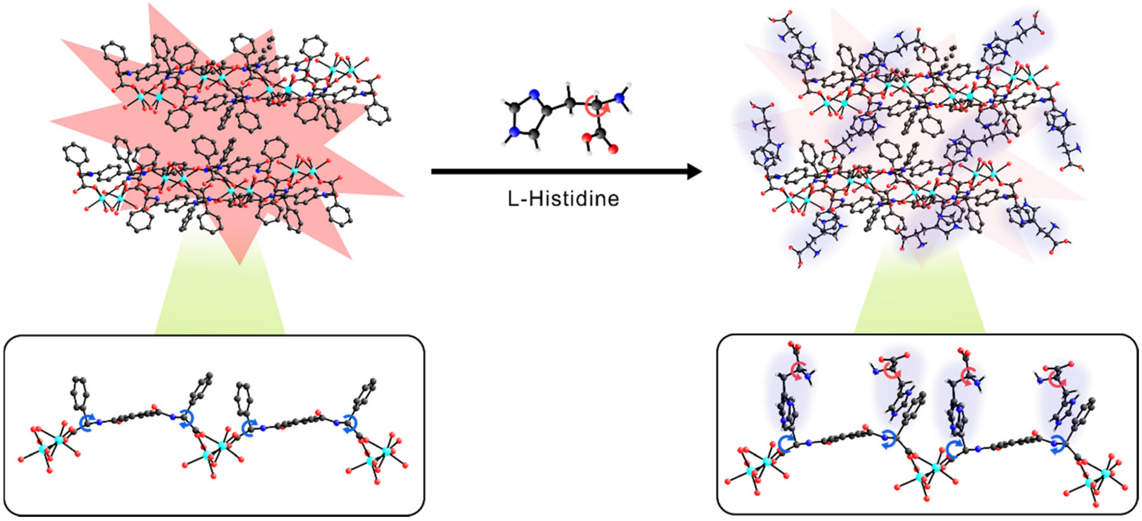

Scheme 1 Schematic illustration of the quenching mechanism by interaction between chiral (*R*)-Zn and the imidazole ring of chiral L-histidine.

Conclusions

In summary, two NCS Zn-based chiral CPs, $[Zn_2((R,R)\text{-TBPG})_2(H_2O)_5]\cdot 4H_2O$ [(*R*)-Zn] and $[Zn_2((S,S)\text{-TBPG})_2(H_2O)_5]\cdot 4H_2O$ [(*S*)-Zn], have been successfully synthesized through mild solvothermal reactions. The title compounds crystallizing in the NCS polar space group, $P2_1$, represent 2D structures consisting of slightly distortive ZnO_6 and the homochiral ligands. Interestingly, the unique bilayer structure is further induced due to the π–π stacking and hydrogen bonding interactions between the two types of layers. (*R*)-Zn and (*S*)-Zn with NCS structures reveal SHG efficiencies of about 0.5 times that of KH_2PO_4 and type-I phase-matching behavior. An unexpected hydrolysis of diethyl ether to ethanol occurred in the presence of (*S*)-Zn, which was confirmed by SC-XRD and GC-MS. The title compounds are very stable in various solvents at various pH values. The water stable homochiral title compounds exhibit excellent enantioselective sensing behavior toward D- and L-histidine. The observed enantioselective discrimination is attributed to the chirality of title compounds as well as the host–guest interactions through the rigid chiral backbones. This study opens a new avenue for the discovery of novel chiral sensors.

Conflicts of interest

There are no conflicts to declare.

Acknowledgements

This research was supported by the National Research Foundation of Korea (NRF) funded by the Ministry of Science and ICT (Grant No. 2018R1A5A1025208 and 2019R1A2C3005530).

Notes and references

1 D. F. Eaton, Nonlinear optical materials, *Science*, 1991, **253**, 281–287.
2 H. Zhang, M. Zhang, S. Pan, X. Dong, Z. Yang, X. Hou, Z. Wang, K. B. Chang and K. R. Poeppelmeier, $Pb_{17}O_8Cl_{18}$: a promising IR nonlinear optical material with large laser damage threshold synthesized in an open system, *J. Am. Chem. Soc.*, 2015, **137**, 8360–8363.
3 K. M. Ok, E. O. Chi and P. S. Halasyamani, Bulk characterization methods for non-centrosymmetric materials: second-harmonic generation, piezoelectricity, pyroelectricity, and ferroelectricity, *Chem. Soc. Rev.*, 2006, **35**, 710–717.
4 Y. Kuk and K. M. Ok, Homochiral three-dimensional noncentrosymmetric lanthanide coordination polymers directed by chiral linkers: syntheses, crystal structures, and optical properties, *CrystEngComm*, 2021, **23**, 3701–3709.
5 J. Kee and K. M. Ok, Hydrogen-Bond-Driven Synergistically Enhanced Hyperpolarizability: Chiral Coordination Polymers with Nonpolar Structures Exhibiting Unusually Strong Second-Harmonic Generation, *Angew. Chem., Int. Ed.*, 2021, **133**, 20824–20828.
6 B. W. Liu, X. M. Jiang, H. Y. Zeng and G. C. Guo, $[ABa_2Cl][Ga_4S_8]$ (A = Rb, Cs): wide-spectrum nonlinear optical materials obtained by polycation-substitution-induced nonlinear optical (NLO)-functional motif ordering, *J. Am. Chem. Soc.*, 2020, **142**, 10641–10645.
7 S. H. Kim, J. Yeon and P. S. Halasyamani, Noncentrosymmetric Polar Oxide Material, Pb_3SeO_5: Synthesis, Characterization, Electronic Structure Calculations, and Structure–Property Relationships, *Chem. Mater.*, 2009, **21**, 5335–5342.
8 Y. Liu, X. Liu, S. Liu, Q. Ding, Y. Li, L. Li, S. Zhao, Z. Lin, J. Luo and M. Hong, An unprecedented antimony (III) borate with strong linear and nonlinear optical responses, *Angew. Chem., Int. Ed.*, 2020, **132**, 7867–7870.
9 X. L. Cao, C. L. Hu, X. Xu, F. Kong and J. G. Mao, $Pb_2TiOF(SeO_3)_2Cl$ and $Pb_2NbO_2(SeO_3)_2Cl$: small changes in structure

induced a very large SHG enhancement, *Chem. Commun.*, 2013, **49**, 9965–9967.

10 E. O. Chi, K. M. Ok, Y. Porter and P. S. Halasyamani, Na2Te3Mo3O16: A new molybdenum tellurite with second-harmonic generating and pyroelectric properties, *Chem. Mater.*, 2006, **18**, 2070–2074.

11 G. Yang, G. Peng, N. Ye, J. Wang, M. Luo, T. Yan and Y. Zhou, Structural modulation of anionic group architectures by cations to optimize SHG effects: a facile route to new NLO materials in the $ATCO_3F$ (A = K, Rb; T = Zn, Cd) series, *Chem. Mater.*, 2015, **27**, 7520–7530.

12 J. Wang, B. Xiong, H. Wu, H. Yu, Z. Hu, J. Wang and Y. Wu, $Bi_{32}Cd_3P_{10}O_{76}$: a new congruently melting nonlinear optical crystal with a large SHG response and a wide transparent region, *Inorg. Chem. Front.*, 2021, **8**, 344–351.

13 Y. C. Hao, X. Xu, F. Kong, J. L. Song and J. G. Mao, $PbCd_2B_6O_{12}$ and $EuZnB_5O_{10}$: syntheses, crystal structures and characterizations of two new mixed metal borates, *CrystEngComm*, 2014, **16**, 7689–7695.

14 G. Zou, G. Nam, H. G. Kim, H. Jo, T. S. You and K. M. Ok, ACdCO3F (A = K and Rb): new noncentrosymmetric materials with remarkably strong second-harmonic generation (SHG) responses enhanced via π-interaction, *RSC Adv.*, 2015, **5**, 84754–84761.

15 G. Zou, Z. Ma, K. Wu and N. Ye, Cadmium-rare earth oxyborates $Cd_4ReO(BO_3)_3$ (Re = Y, Gd, Lu): congruently melting compounds with large SHG responses, *J. Mater. Chem.*, 2012, **22**, 19911–19918.

16 L. Huang, G. Zou, H. Cai, S. Wang, C. Lin and N. Ye, $Sr_2(OH)_3NO_3$: the first nitrate as a deep UV nonlinear optical material with large SHG responses, *J. Mater. Chem. C*, 2015, **3**, 5268–5274.

17 W. Seo and K. M. Ok, Novel noncentrosymmetric polar coordination compounds derived from chiral histidine ligands, *Inorg. Chem. Front.*, 2021, **8**, 4536–4543.

18 H. Choi and K. M. Ok, Systematic centricity control using a chiral template: novel noncentrosymmetric polar niobium oxyfluorides and tantalum fluorides directed by chiral histidinium cations, [(L-hisH$_2$)NbOF$_5$], [(D-hisH$_2$)NbOF$_5$], [(L-hisH$_2$)TaF$_7$], and [(D-hisH$_2$)TaF$_7$], *Inorg. Chem. Front.*, 2021, **8**, 3843–3850.

19 H. Jo, X. Chen, H. S. Lee and K. M. Ok, Chiral Template-Driven Macroscopic Chirality Control: Structure-Second-Harmonic Generation Properties Relationship, *Eur. J. Inorg. Chem.*, 2021, 426–434.

20 M. Liu, H. S. Quah, S. Wen, J. Wang, P. S. Kumar, G. Eda, J. J. Vittal and W. Ji, Nonlinear optical properties of a one-dimensional coordination polymer, *J. Mater. Chem. C*, 2017, **5**, 2936–2941.

21 Y. Kuk and K. M. Ok, Novel enantiomorphic Pb-coordination polymers dictated by the corresponding chiral ligands, [Pb((R,R)-TBA)(H2O)]·1.7H2O and [Pb((S,S)-TBA(H2O)]·1.7H2O [TBA = 1,3,5-triazin-2(1H)-one-4,6-bis(alanyl)], *Mater. Chem. Front.*, 2021, **5**, 1330–1340.

22 C. Wang, T. Zhang and W. Lin, Rational synthesis of noncentrosymmetric metal–organic frameworks for second-order nonlinear optics, *Chem. Rev.*, 2012, **112**, 1084–1104.

23 C. Gao, J. Zhou, M. Cui, D. Chen, L. Zhou, F. Li and X.-L. Li, Distinct nonlinear optical responses in three pairs of 2D homochiral Ag (I) enantiomers modulated by dicarboxylic acid ligands, *Inorg. Chem. Front.*, 2022, **9**, 284–293.

24 S. Kitagawa, R. Kitaura and S. I. Noro, Functional porous coordination polymers, *Angew. Chem., Int. Ed.*, 2004, **43**, 2334–2375.

25 H. Tang, K. Yang, K. Y. Wang, Q. Meng, F. Wu, X. Wu, Y. Li, W. Zhang, Y. Luo and C. Zhu, Engineering a homochiral metal–organic framework based on an amino acid for enantioselective separation, *Chem. Commun.*, 2020, **56**, 9016–9019.

26 J. Duan, Q. Li and Z. Lu, A new mesoporous coordination polymer: synthesis, structure, and gas adsorption studies, *CrystEngComm*, 2015, **17**, 2087–2090.

27 K. Biradha, A. Goswami and R. Moi, Coordination polymers as heterogeneous catalysts in hydrogen evolution and oxygen evolution reactions, *Chem. Commun.*, 2020, **56**, 10824–10842.

28 J. Duan, W. Jin and S. Kitagawa, Water-resistant porous coordination polymers for gas separation, *Coord. Chem. Rev.*, 2017, **332**, 48–74.

29 A. Sun, Y. Yang, Y. Liu, L. Ding, P. Duan, W. Yang and Q. Pan, A Zinc Coordination Polymer Sensor for Selective and Sensitive Detection of Doxycycline Based on Fluorescence Enhancement, *Cryst. Growth Des.*, 2021, **21**, 4971–4978.

30 J. D. Kopple and M. Swendseid, Evidence that histidine is an essential amino acid in normal and chronically uremic man, *J. Clin. Investig.*, 1975, **55**, 881–891.

31 L. Fabbrizzi, G. Francese, M. Licchelli, A. Perotti and A. Taglietti, Fluorescent sensor of imidazole and histidine, *Chem. Commun.*, 1997, 581–582.

32 G. Patel and S. Menon, Recognition of lysine, arginine and histidine by novel p-sulfonatocalix [4] arene thiol functionalized gold nanoparticles in aqueous solution, *Chem. Commun.*, 2009, 3563–3565.

33 Y. Zhou, S. Wang, K. Zhang and X. Jiang, Visual detection of copper (II) by azide-and alkyne-functionalized gold nanoparticles using click chemistry, *Angew. Chem., Int. Ed.*, 2008, **47**, 7454–7456.

34 A. Spek, Single-crystal structure validation with the program PLATON, *J. Appl. Crystallogr.*, 2003, **36**, 7–13.

35 G. Socrates, *Infrared and Raman characteristic group frequencies: tables and charts*, John Wiley & Sons, 2004.

36 P. Kubelka, Ein Beitrag zur Optik der Farbanstriche (Contribution to the optic of paint), *Z. Tech. Phys.*, 1931, **12**, 593–601.

37 P. G. Jiang, P. Zhang, Y. Gong and J. H. Lin, Photocurrent-generating properties of bulk and few-layered Cd (II) coordination polymers based on a rigid dicarboxylate ligand, *Dalton Trans.*, 2016, **45**, 4603–4613.

38 X. Yan, X. Qiu, Z. Yan, H. Li, Y. Gong and J. Lin, Configurations, band structures and photocurrent responses of

4-(4-oxopyridin-1 (4H)-yl) phthalic acid and its metal-organic frameworks, *J. Solid State Chem.*, 2016, **237**, 313–322.

39 J. P. Perdew, Density functional theory and the band gap problem, *Int. J. Quantum Chem.*, 1985, **28**, 497–523.

40 J.-H. Deng, J. Luo, Y.-L. Mao, S. Lai, Y.-N. Gong, D.-C. Zhong and T.-B. Lu, π–π stacking interactions: Non-negligible forces for stabilizing porous supramolecular frameworks, *Sci. Adv.*, 2020, **6**, eaax9976.

41 C. Fan, K. W. Plaxco and A. J. Heeger, High-efficiency fluorescence quenching of conjugated polymers by proteins, *J. Am. Chem. Soc.*, 2002, **124**, 5642–5643.

42 S. Thoonen, H. M. Tay and C. Hua, A chiral binaphthyl-based coordination polymer as an enantioselective fluorescence sensor, *Chem. Commun.*, 2022, **58**, 4512–4515.

43 Q. Zhang, M. Lei, F. Kong and Y. Yang, A water-stable homochiral luminescent MOF constructed from an achiral acylamide-containing dicarboxylate ligand for enantioselective sensing of penicillamine, *Chem. Commun.*, 2018, **54**, 10901–10904.

44 X. Wu, X. Han, Q. Xu, Y. Liu, C. Yuan, S. Yang, Y. Liu, J. Jiang and Y. Cui, Chiral BINOL-based covalent organic frameworks for enantioselective sensing, *J. Am. Chem. Soc.*, 2019, **141**, 7081–7089.

45 M. M. Wanderley, C. Wang, C. D. Wu and W. Lin, A chiral porous metal–organic framework for highly sensitive and enantioselective fluorescence sensing of amino alcohols, *J. Am. Chem. Soc.*, 2012, **134**, 9050–9053.

46 M. Lei, X. Wang, T. Zhang, Y. Shi, J. Wen and Q. Zhang, Homochiral Eu^{3+}@MOF Composite for the Enantioselective Detection and Separation of (*R*/*S*)-Ornidazole, *Inorg. Chem.*, 2022, **61**, 6764–6772.

47 P. Chandrasekhar, A. Mukhopadhyay, G. Savitha and J. N. Moorthy, Remarkably selective and enantiodifferentiating sensing of histidine by a fluorescent homochiral Zn-MOF based on pyrene-tetralactic acid, *Chem. Sci.*, 2016, **7**, 3085–3091.